Contents lists available at ScienceDirect

Applied Catalysis B: Environmental

Fast electron transfer and enhanced visible light photocatalytic activity using multi-dimensional components of carbon quantum dots@3D daisy-like In$_2$S$_3$/single-wall carbon nanotubes

Jinze Li [a,c], Yue Ma [a,c], Zhefei Ye [a], Mingjun Zhou [a], Huiqin Wang [b], Changchang Ma [b], Dongdong Wang [a], Pengwei Huo [a,c,*], Yongsheng Yan [a,c,*]

[a] School of Chemistry & Chemical Engineering, Jiangsu University, Zhenjiang 212013, People's Republic of China
[b] School of Environment, Jiangsu University, Zhenjiang 212013, People's Republic of China
[c] Institute of Green Chemistry and Chemical Technology, Jiangsu University, Zhenjiang 212013, People's Republic of China

ARTICLE INFO

ABSTRACT

One of current ideal thought to reduce the recombination of photogenerated electrons and holes from semiconductors is constructing Multi-dimensional semiconductor-carbon (S-C) heterostructures. As well as acting to photo-degrade the organic contaminant and decrease the toxicity, β-In$_2$S$_3$ is chosen as a potential semiconductors for photocatalysts. Relative good photocatalytic properties delivered on β-In$_2$S$_3$, however, the fast recombination of photogenerated charge carriers are often appeared, causing reduced further application. Carbon quantum dots (CQDs) involve the introduction of plasma effect into the zero-dimensional nanomaterials in order to arouse an effect: either promoting the charge carriers transfer or plasma energy conversion of the photo-excited CQDs. However, state of the two components also encompass the poor quantum yield existed in the CQDs by its serious agglomeration. Thereby, the delivery of extraordinary ballistic electrical and thermal conductivity on single-walled carbon nanotubes (SWNTs), have shown potential for use in a variety of semiconductors decorating application. Herein, we show that a novel CQDs@In$_2$S$_3$/SWNTs composite in the Multi-dimensional (3D) hierarchical superstructures with an enhanced photocatalytic efficiency. The ESR analysis and free radicals trapping experiments indicated that the O$_2$•$^-$ and h$^+$ were the main active species for the photocatalytic degradation. The potential photocatalytic mechanism of the three components is discussed and the direction in the plasma effect exhibited in CQDs is also considered, with a particular focus on photocatalytic area.

© 2016 Elsevier B.V. All rights reserved.

1. Introduction

Environmental pollution and energy shortage are the two hot issues in the world during the past recent decade. Organic and toxic pollutants are harmful for human health and hinder sustainable development, in especial antimicrobial agents pollution that primarily caused by the rapid development of pharmaceutical industries and modern medical technology is now a major crisis for public health agencies [1]. As one of the most promising solutions for the degradation of various kind of antibiotics contaminants, semiconductor-based heterogeneous photocatalysis have received tremendous attention as it is a green technology for decompos-ing water into oxygen and hydrogen, completely eliminating all kinds of contaminants and inactivating bacteria and viruses under the illumination of sunlight, thus holding great promise to achieve the purpose of benefiting the worldwide energy and environmental issues [2,3]. Various of semiconductors including metal oxides, sulfides, halide, organic metal complexes and other metal-free photocatalyst, such as titanium dioxide [4], iron oxide, zinc oxide [5,6], cadmium selenide [7] and graphitic carbon nitride [8–10] have been widely investigated and utilized in numerous photocatalytic applications for degradation of organic pollutants, photocatalytic conversion of CO$_2$ and the photocatalytic splitting of water for H$_2$ production [10–15].

Among these common and popular semiconductors, Indium sulfide (In$_2$S$_3$) as a fascinating and promising material which is the n-type III–VI group chalcogenide semiconductor with a band gap of 2.0–2.2 eV, has attracted intensive study enthusiasm [16,17]. It is known that β-In$_2$S$_3$ (spinel structure, stable up to 1027 K) is

the thermodynamically stable phase exhibiting outstanding opto-electronic performances and has been widely investigated as an excellent visible-light-driven (VLD) photocatalyst and photosensitizer for a relatively narrow band gap semiconductor because of its defected spinel structure [17,18]. Based on these properties, the applications of β-In_2S_3 have been expanded in many field not only photocatalytic degradation of organic contaminant. For example, it was reported that solar cell devices prepared by using β-In_2S_3 as a buffer layer provided 16.4% fractional conversion which close to that of the standard CdS buffer layer [19]. Furthermore, in recent years, more and more researchers have reported that the Cd^{2+} has been taken over by In^{3+} ions because of its much lower toxicity, suggesting reduction of secondary pollution for water pollution measures [20]. However, similar to other narrow band gap VLD photocatalysts, it is still an arduous challenge to overcome the phenomenon of poor quantum yield which accused by the rapid recombination of photogenerated electron-hole pairs. To date, a number of attempts have been made to hinder the recombination rate of photogenerated electron-hole pairs to form semiconductor heterostructure by combining In_2S_3 via coupling with other charge acceptor and carrier, such as the nanostructures of the modified noble metals to induce surface plasmon resonance (SPR) [21], the matched band structure semiconductors [11] and carbon materials [17,21,22], that corresponding design and fabrication of semiconductor-metal (S-M) heterostructure, semiconductor–semiconductor (S-S) heterostructure and semiconductor-carbon (S-C) heterostructure, respectively [23]. Among them, carbon materials attract tremendous interest because of their superior electroconductivity, excellent physicochemical stability, high absorption properties, and so on. Additionally, it is still necessary to design novel VLD heterostructure photocatalysts systems to prolong the lifetimes of photogenerated electron-hole pairs and expand the limited visible light absorption band, such as multicomponent heterostructures, in which two or more photo-responsive components and electron-transfer system are spatially integrated, with the aim of improving the photocatalytic efficiencies for ever-increasing requirements of future energy and environmental technologies [23–25].

Over the past few years, the increasing amount of star carbon materials have stepped into researchers' attention spans in the large carbon family for photocatalytic applications, such as graphene [3,26], carbon nanofibers [27], carbon nanotubes [28,29], biochar [30] and so on. Among these known carbon nanomaterials, carbon quantum dots (CQDs), as a novel and ecofriendly nano-carbon material constitute a relatively new class of zero-dimensional nanostructures with sizes typically 2–10 nm in diameter, predominantly consist of amorphous or turbostratic carbon together with nanocrystalline regions of sp^2-hybridized graphitic carbon or graphene and graphene oxide sheets fused by diamond-like sp^3-hybridized carbon insertions [31,32], has attracted most recent notice for applications in sensing, bioimaging, optoelectronics, drug delivery, medical diagnosis, photovoltaic devices photocatalysis and electrocatalysis, owing to their biocompatibility, low toxicity, stable, tunable and strong photoluminescence (PL) properties [33–36]. Not only the down-converted PL, CQDs also exhibit excellent up-converted [37], which enable CQDs to take full advantage of the spectrum of sunlight attribute to conjugated π-domains [38] and PL emissions related to structural and edge or surface defects [39] which is highly beneficial for photocatalytic reactions, in particular present in CQDs contribute to their multicolor emissions that are concentrated in the blue and green regions of the visible light spectrum [33,40]. A series of photocatalytic experiments confirmed that the photocatalytic activity of introducing CQDs can be effectively improved by visible light, which may be attributed to their function photoinduced electron-accepting properties. Furthermore, the emissions

of such passivated CQDs covered a broad range of the visible region and extended into the near-infrared (NIR) region [41]. Due to the stable PL and excellent photoinduced electron transfer/reservoir properties of CQDs [33,42], CQDs have been combined with other semiconductors successfully contributed to enhance the photocatalytic activity both for contaminant degradation and hydrogen generation, and forming a heterostructure by combining CQDs with noble metal, carbon nanomaterials and/or other semiconductor have been eagerly employed to improve the photocatalytic efficiencies of photocatalysts very recently, such as Au@CQDs [43], CQDs/CNTs [44], CQDs/TiO_2 [45], CQDs/Fe_2O_3 [46], CQDs/g-C_3N_4 [32], CQDs/BiOX [47] and CQDs/Cu_2O [34]. Similarly, as an excellent adsorption carbon material for organic toxic chemicals, the single-walled carbon nanotubes (SWNTs) have been utilized as the vectorial charge transfer of carriers in our system. Moreover, about one third of all possible SWNTs exhibit metallic properties and the rest two-third are inclined to act as semiconductors [48]. To date, more and more studies have focused on coupling SWNTs with other semiconductors which possessed appropriate band gap, due to their unique properties like heterostructure or photosensitization, for these photocatalysts could efficiently widen light response range by photosensitization effect of carbon nanotubes and minimize recombination tendency of electron-hole pairs by Schottky barrier between semiconductors and carbon nanotubes [49], such as TiO_2/CNTs [28,50], MWNT-TiO_2-SiO_2 [51], Ag/AgX-CNTs (X = Cl, Br, I) [52] and Ag/Ag_2O/SWNTs [53]. However, it is difficult to take full advantage of SWNTs because of their lengthiness, twine, agglomeration, low surface activity and poor dispersion in water or most organic solvents, which severely restricted their applications [54]. Previous studies have indicated that chemical functionalization of the open ends and walls of SWNTs would play a vital role in optimizing their properties. It is quite essential for the chemical "functionalizing" and physical "shortening" of SWNTs [55,56]. Herein, the improved Ziegler's method [57] has been used to cut the highly entangled long ropes of SWNTs into short, open-ended pipes. As a result of the physicochemical treatment of SWNTs, the ends and sometimes the sidewalls of the nanotubes have been modified by oxygen containing groups, which has significant implications for electronic and thermal properties of these "semiconducting" carbon materials.

There are some few extraordinary superiorities of multi-dimensional component of composite materials in photocatalysis, especially the heterostructure materials [11,25,58]. However, there have been few researches to study the multi-dimensional component of photocatalytic composite materials up to now. On the basis of the above consideration, we fabricated novel zero-dimensional CQDs modified three-dimensional In_2S_3 nanoflowers via a hydrothermal approach and the treated one-dimensional SWNTs have been added during the formation of CQDs@In_2S_3 simultaneously. The self-assembly of the prepared CQDs@In_2S_3/SWNTs which into multi-dimensional hierarchical superstructures via a feasible route for fabricating heterostructure nanomaterials. In this multicomponent heterostructure system, the CQDs served as the bridge for carrying and transferring electron between In_2S_3 and SWNTs, which have efficiently linked/united three parts of the composite materials and finally fabricated this multi-dimensional components of a CQDs@In_2S_3/SWNTs that consisted of CQDs/In_2S_3 and In_2S_3/SWNTs S-C heterostructures. Furthermore, as a group of newly emerged fluorescent nanomaterials, the unique metalloid plasma and PL up-conversion effect of CQDs presented the energy conversion of electronic energy and thermal energy of the photo-excited CQDs during the photocatalytic process [34,37,42]. To the best of our knowledge, there is no report in literature on the fabrication of multi-dimensional component heterostructure of all the CQDs, In_2S_3 and SWNTs. The photocatalytic activities of CQDs@In_2S_3/SWNTs catalysts are evaluated by the photocatalytic

degradation of three different kinds of model antibiotic pollutants. The mechanism of contaminant photodegradation in this system is studied via using free radicals trapping experiments and ESR analysis.

2. Experimental section

2.1. Materials

Indium chloride tetrahydrate ($InCl_3 \cdot 4H_2O$), thioacetamide (C_2H_5NS, TAA), citric acid ($C_6H_8O_7$), ethylenediamine ($C_2H_8N_2$), nitric acid (HNO_3, 65%), sulfuric acid (H_2SO_4, 70%), ethanol (C_2H_5OH) were all supplied by Sinopharm Chemical Reagent Co., Ltd. (Shanghai, China). Single-walled carbon nanotubes (SWNTs) were purchased from Beijing WuYuan Biotechnology Co., Ltd. Ciprofloxacin (CIP), tetracycline (TC) and Levofloxacin (LEV) were purchased from Shanghai Shunbo Biological Engineering Co. Ltd. All of the materials were analytical grade for synthesis and used as received without further purification. Deionized water was used throughout this work from local sources.

2.2. Synthesis of daisy-like In_2S_3 with hierarchical 3D architectures

In a typical procedure, $InCl_3 \cdot 4H_2O$ (0.5 mmol) and L-cysteine (1.5 mmol) were dissolved in 50 mL of deionized water, and the mixture was dispersed to form a homogeneous solution under vigorous constant stirring for 20 min. Then, the pH of solution was adjusted to 8 with dropwise addition of 1 M NaOH solution. The mixture was transferred to a 60 mL Teflon-lined stainless steel autoclave and maintained at 180 °C for 10 h. After cooling to room temperature, the orange precipitates of In_2S_3 was collected, washed with distilled water and absolute ethanol several times, and then dried in vacuum at 60 °C for 12 h. Finally, the as-prepared solid powder samples were loaded into a quartz boat and annealed in a tube furnace at 400 °C for 10 min under argon atmosphere; it was then cooled down to room temperature naturally. The heating rate for the tube furnace was 10 °C/min before the furnace temperature reached 400 °C.

2.3. Synthesis of Carbon Quantum Dots (CQDs)

The CQDs were synthetized by the "bottom-up" approaches which using a microwave heating route as follows: citric acid (1.0507 g) and ethylenediamine (0.45 g) was dissolved in deionized water (10 mL) under vigorous stirring for 30 min and then put into ultrasonic machine during 5 min. The solution was transferred to a domestic microwave oven at 800W for 10 min. After cooling down to room temperature by water or naturally, the product, which was light-yellow and transparent, was subjected to dialysis for 24 h in order to obtain CQDs. The resultant solution was sealed and stored in dry and cool place for subsequent synthesis.

2.4. Synthesis of CQDs@In_2S_3/SWNTs composites

Before the synthesis of composites sample, the highly entangled long ropes of SWNTs was cut via improved Ziegler's method as follows: The 0.5 g SWNTs was disperse in the concentrated 3:1H_2SO_4/HNO_3 mixtures during ultrasonic treatment at 55 °C for 3 h. After washing and collecting, the treated SWNTs was obtained.

The CQDs@In_2S_3/SWNTs hybrid materials were synthesized via a one-pot hydrothermal method. In a typical procedure, a certain amount of as-prepared CQDs and shorted SWNTs were simultaneously introduced during the preparation of In_2S_3. The rest of the steps were same as the fabrication of In_2S_3. Finally, a series of CQDs@In_2S_3/SWNTs nanocomposites with different amounts

addition ratios of CQDs and SWNTs to In_2S_3 were obtained. The formation mechanism of CQDs@In_2S_3/SWNTs nanomaterial is proposed in Scheme 1.

2.5. Characterization methods and instrumentation

The crystal structure was analyzed by the powder X-ray diffraction (XRD model MAC Science, Japan) with Ni-filtrated Cu-Kα radiation. The scan range of 2θ was 5–80° at a scan rate of 5°/min. The X-ray photoelectron spectroscopy (XPS) measurements were measured on a PerkinElmer PHI 5300 instrument with a monochromatic Mg Kα source to test the elements on the surface of nanomaterials and the C1 s signal was set to the position of 284.6 eV. The transmission electron microscopy (TEM), high-resolution transmission electron microscopy (HR-TEM) images and corresponding selected area electron diffraction (SAED) pattern were examined by transmission electron microscopy (JEM-2010, Japan). The scanning electron microscopy (SEM) figures were characterized by a field emission scanning electron microscopy (FE-SEM, JSM-7001F, Japan). Energy dispersive X-ray spectroscopy (EDS) was taken on a FEI Tecnai G2F20 instrument and operated at an accelerating voltage of 200 kV. The diffuse reflectance spectra (DRS) of the catalysts were performed in the range of 250–850 nm using a UV–vis spectrophotometer (UV-2450; Shimazu, Japan) equipped with an integrating sphere. The photoluminescence (PL) spectra for solid samples were performed by an F-4500 (Hitachi, Japan) photoluminescence detector. Specific surface area was detected by the Brunauer-Emmett-Teller (BET) technique from the N_2 adsorption isotherm, the pore size distribution was determined by desorption isotherm using the Barrett-Joiner-Halenda (BJH) method.

2.6. Photoelectrochemical measurements

Incident-photon-to-current conversion efficiencies (IPCE) were calibrated with an electrochemical system (CHI 660B, Shanghai, China) using a standard three-electrode quartz cells with 0.5 M Na_2SO_4 electrolyte solution, a Pt wire and a saturated calomel electrode (SCE) were used as the counter electrode and the reference electrodes. The process of preparing the working electrode according to our previous research [5]. Electrochemical impedance spectroscopy (EIS) was performed in a 0.5 M Na_2SO_4 solution with a frequency range from 0.1 Hz to 100 kHz at 0.5 V. The amplitude of applied sine wave potential in each case was 5 mV which was carried out using a ZENNIUM electrochemical workstation (Zahner Instruments, Germany), and all electrochemical signals were recorded by a CHI660 B electrochemical analyzer (Chen Hua Instruments, Shanghai, China). All electrodes were same as the electrodes using in IPCE.

2.7. Electron spin resonance (ESR) spectroscopy

ESR was introduced to characterize the formation of $O_2 \bullet^-$, $^\bullet OH$ and $1O_2$ which were carried on a Brucker A300 ESR spectrometer at room temperature; the ESR signals of spin-trapped paramagnetic species was verified with 5,5-diamethyl-1-pyrroline N-oxide (DMPO) and 4-oxo-2,2,6,6-tetramethyl (4-oxo-TEMP) [59]. The involvement of $^\bullet O_2^-$ was detected in methanol due to the instability of $^\bullet O_2^-$ in water, and the involvement of $^\bullet OH$ was examined in ultrapure water [60]. Fifty microliter aliquots of sample solutions were put into the quartz capillary tubes with internal diameters of 0.9 mm. After The quartz capillary tubes were inserted into the ESR cavity after sealed. The spectra were recorded during a 450 W xenon lamp solar simulator irradiation at selected times.
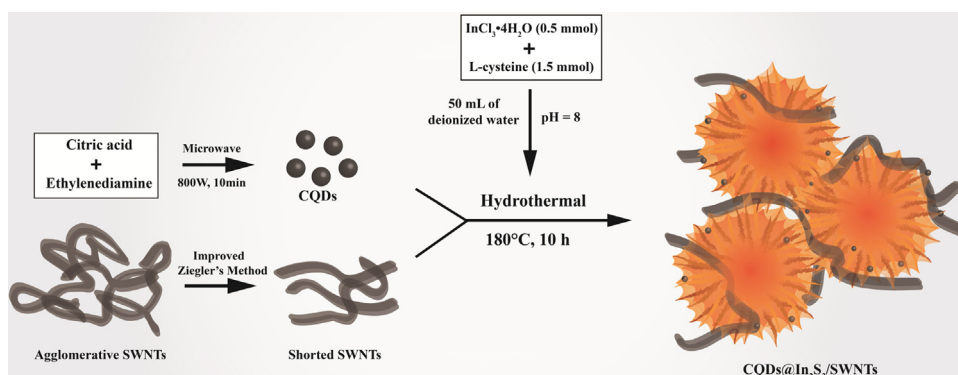
Scheme. 1. Schematic illustration of the formation of CQDs@In$_2$S$_3$/SWNTs in the whole synthetic process.

2.8. Photocatalytic activity test

To compare the photocatalytic activities of pure In$_2$S$_3$, In$_2$S$_3$/SWNTs and synthesized CQDs@In$_2$S$_3$/SWNTs composites with different contents, a series of the level of photodegradation were evaluated by using CIP (10 mg L^{-1}), TC (20 mg L^{-1}) and LEV (15 mg L^{-1}) solutions as target pollutants under visible-light irradiation. A 350 W Xenon arc lamp was used as the light source of the photocatalytic reaction. Briefly, the photochemical reactor system contains 100 mL of CIP, TC and LEV solution respectively and 0.08 g of photocatalysts with recycling water (25 °C) to maintain a constant reactor temperature. The mixture was stirred under dark conditions for 30 min to ensure that the adsorption-desorption balance was reached. Samples were taken from the suspension at a given 10 min interval and centrifugally separated to remove photocatalysts for cyclic utilization in additions runs. The concentration of CIP, TC and LEV were measured via a UV–vis spectrophotometer at a wavelength of 276 nm, 357 nm and 287 nm, respectively.

3. Results and discussion

3.1. Structures and surface compositions

Fig. 1 shows the X-ray diffraction (XRD) patterns of the samples with different compositions synthesized at 180 °C for 10 h. As shown in Fig. 1a, the distinct peaks located at ca. 14.3°, 27.4°, 28.7°, 33.2°, 43.6°, 47.7°, 56.5° and 59.4° are indexed to the (111), (311), (222), (400), (511), (440), (622), (444) crystal planes of cubic In$_2$S$_3$ phase (β-In$_2$S$_3$) (JPCDS No. 65-0459), respectively. A relatively weak appeared at ca. 26° is corresponding to the characteristic peaks of C which owing CQDs [35,61]. Moreover, the similarity between the crystal structures of the samples suggests that hybrid with CQDs does not obviously change the crystalline structure of the CQDs@In$_2$S$_3$/SWNTs compound, which is probably ascribe to the similar lattice fringe spacings of (002) crystal plane of CQDs (3.25 Å) and (311) plane of cubic In$_2$S$_3$ (3.21 Å) [17,18]. As shown in Table 1, the average crystallite sizes of In$_2$S$_3$, In$_2$S$_3$/SWNTs and CQDs@In$_2$S$_3$/SWNTs samples calculated from the (311) peak of XRD pattern by Scherrer formula ($D = K\gamma / B\cos\theta$) [62] are about 11.55 nm, 8.88 nm and 9.04 nm, respectively. We can see from Fig. 1b that with the increasing amount of CQDs, the intensity of β-In$_2$S$_3$ have weaken gradually. No other impure phases are observed of the XRD patterns, indicating a high purity of the as-synthesized products.

The surface chemical composition and valence states of various elements in CQDs@In$_2$S$_3$/SWNTs sample, and the interaction between In$_2$S$_3$ and CQDs were analyzed by X-ray photoelectron spectroscopy (XPS) in Fig. 2. The survey scan spectrum (Fig. 2a) indicates the presence of In, S and C in the sample. As shown in Fig. 2b,

the high resolution scanning XPS spectrum of In 3d with two symmetrical peaks at the binding energies of 444.2 eV and 451.9 eV for In 3d$_{5/2}$ and In 3d$_{3/2}$, respectively [20]. The S 2p core level spectra (Fig. 2c) represent the peaks at 161.2 eV and 162.5 eV would be attributed to S 2p$_{3/2}$ and S 2p$_{1/2}$ transitions, respectively [63]. Fig. 2d shows the high-resolution XPS spectra of C 1s. The main peak at 284.6 eV is ascribed to the C—C bond with graphitic carbons (sp^2 orbital) which is identified as originating from the amorphous carbon phase or adventitious carbon [33]; the peaks at 286.1, 287.6 and 289 eV are attributed to alcoholic carbons (C—O), carbonyl carbons (C=O), and carboxyl carbons (O—C=O), respectively [42,64]. Interestingly, the peak of the carboxyl carbon (O—C=O) in our work is found to shift obviously to a lower binding energy, suggesting that the carboxyl acts as a nucleation site for CQDs and In$_2$S$_3$ nanoflowers on SWNTs [34,65]. The result of XPS analysis reveals the coexistence of In$_2$S$_3$ and CQDs in CQDs@In$_2$S$_3$/SWNTs composite photocatalysts.

3.2. Morphology and X-EDS analysis

The morphology and structure of the as-prepared materials were revealed by FESEM, TEM, HR-TEM and SAED. The overall SEM morphology of flower-like In$_2$S$_3$, In$_2$S$_3$/SWNTs and CQDs@In$_2$S$_3$/SWNTs were shown in Fig. S1. Fig. 3 shows the TEM images of daisy-like β-In$_2$S$_3$, CQDs, CQDs/In$_2$S$_3$ and as-prepared CQDs@In$_2$S$_3$/SWNTs, respectively. As shown in Figs. 3 a and 1 b, the daisy-like structure of β-In$_2$S$_3$ sample prepared at 180 °C for 10 h which hold a complete and uniform morphology with the average diameter about 500 nm. Fig. 3c shows the TEM image of the CQDs which illustrated that the as-prepared C-dots with a spherical shape and the diameters of 2 − 5 nm, were uniform and monodisperse. Also, as shown in HR-TEM image (Fig. 3i) indicate that for the typical CQDs, the lattice spacing of the CQDs was about 3.25 Å which corresponding to the 002facet of CQDs [66]. Fig. 3d and e are TEM images of CQDs/In$_2$S$_3$ composite. Compared with the pure β-In$_2$S$_3$ (Fig. 3a and b) with a smooth and transparent crystal edges, it can be obviously seen that a large number of CQDs are evenly grown to the surface and interior of In$_2$S$_3$ nanoflowers to form a S-C heterostructure, which is a strong evidence for explaining the formation of CQDs/In$_2$S$_3$ heterostructure. Meanwhile, the CQDs/In$_2$S$_3$ hybrid material has the similar daisy-like morphology, indicating that the introduction of CQDs to In$_2$S$_3$ did not change the main structure. Fig. 3f–h implies the CQDs@In$_2$S$_3$/SWNTs composite. As shown in Fig. 3f, we can see an entire morphology of CQDs@In$_2$S$_3$/SWNTs and the shorted SWNTs were obviously grafted around the as-prepared globular flowers. A closer observation is shown in Fig. 3g and h is the partial enlarged detail of the selected area in Fig. 3g, indicating the detailed structures of these hybrid materials. It can be clearly seen that the CQDs are successfully loaded on both the surface of
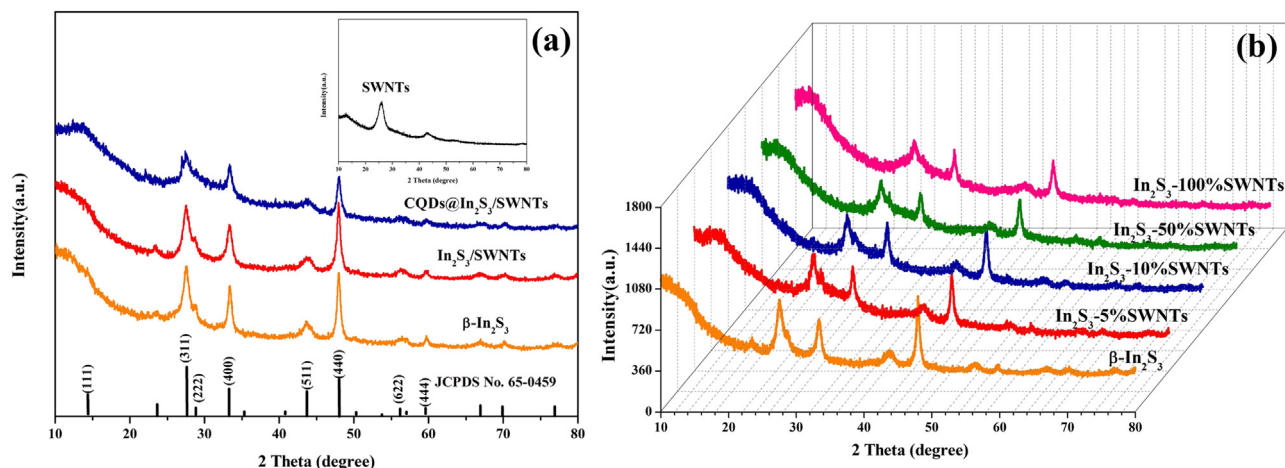
Fig. 1. XRD patterns of the as-prepared materials: (a) pristine β-In$_2$S$_3$, In$_2$S$_3$/SWNTs and CQDs@In$_2$S$_3$/SWNTs composites, (inset) pure SWNTs; (b) CQDs/In$_2$S$_3$ with different CQDs amount.

Table 1
Crystallite size, morphology, BET Surface Area and band gap of pure SWNTs, β-In$_2$S$_3$, In$_2$S$_3$/SWNTs and CQDs@In$_2$S$_3$/SWNTs Samples.

Sample	Morphology	Crystallite size (Scherrer equation) (nm)	Pore volume (BJH method) (cm^3 g^{-1})	Pore diameter (nm)	BET surface area (m^2 g^{-1})	Band gap (Kubelka-Munk function) (eV)
SWNTs	nanotubes	–	0.566	3.832	324.752	–
β-In$_2$S$_3$	nanoflowers	11.55	0.197	3.851	40.637	2.05
In$_2$S$_3$/SWNTs	flowers + tubes	8.88	0.266	3.837	78.354	1.87
CQDs@ In$_2$S$_3$/SWNTs	dots + flowers + tubes	9.04	0.285	3.814	82.276	1.75
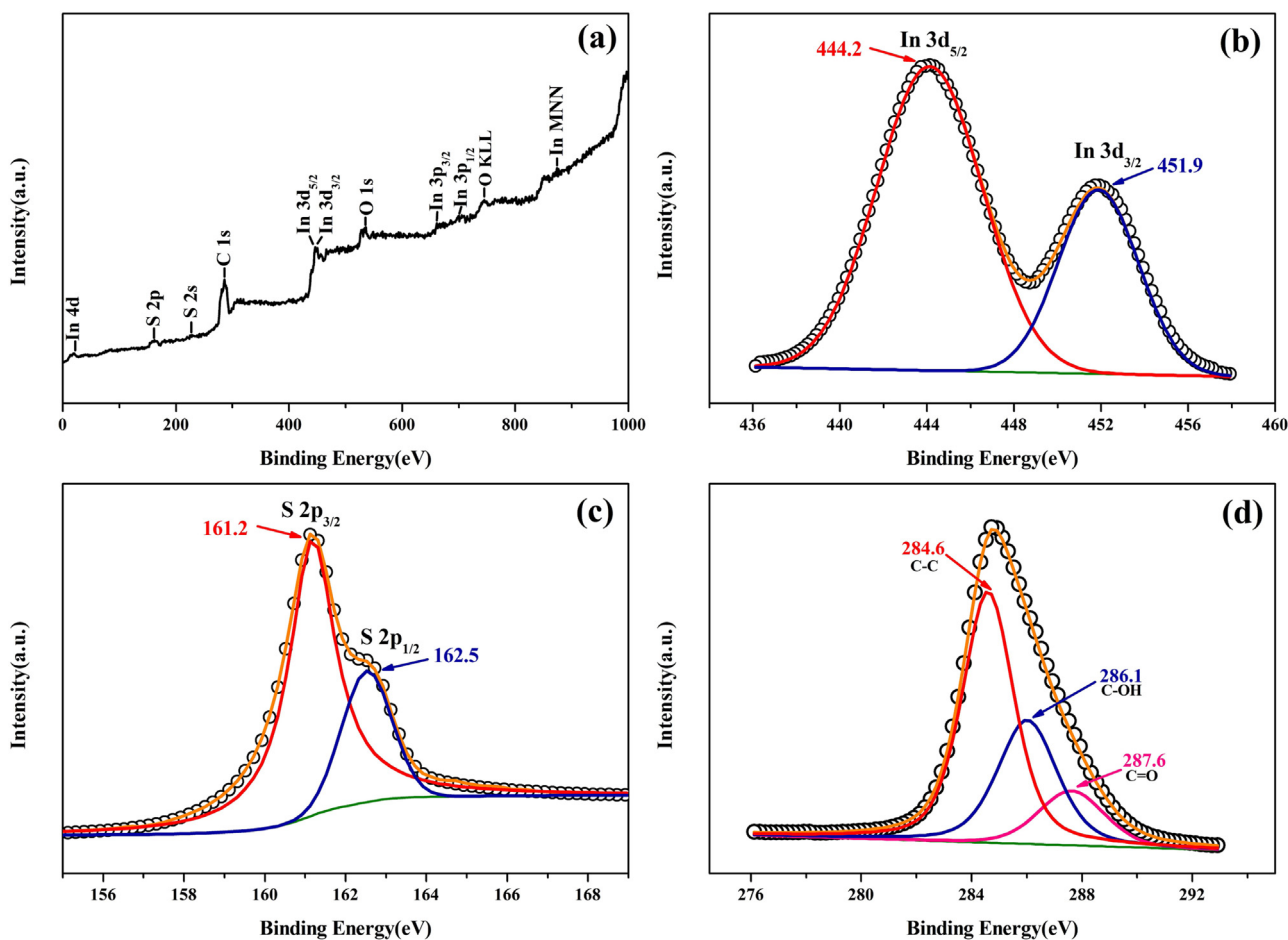
Fig. 2. XPS data from the surface of the sample: (a) the whole-range spectrum of CQDs@In$_2$S$_3$/SWNTs; (b) In 3d core-level spectrum; (c) S 2p core-level spectrum; (d) C 1 s of core-level spectrum.
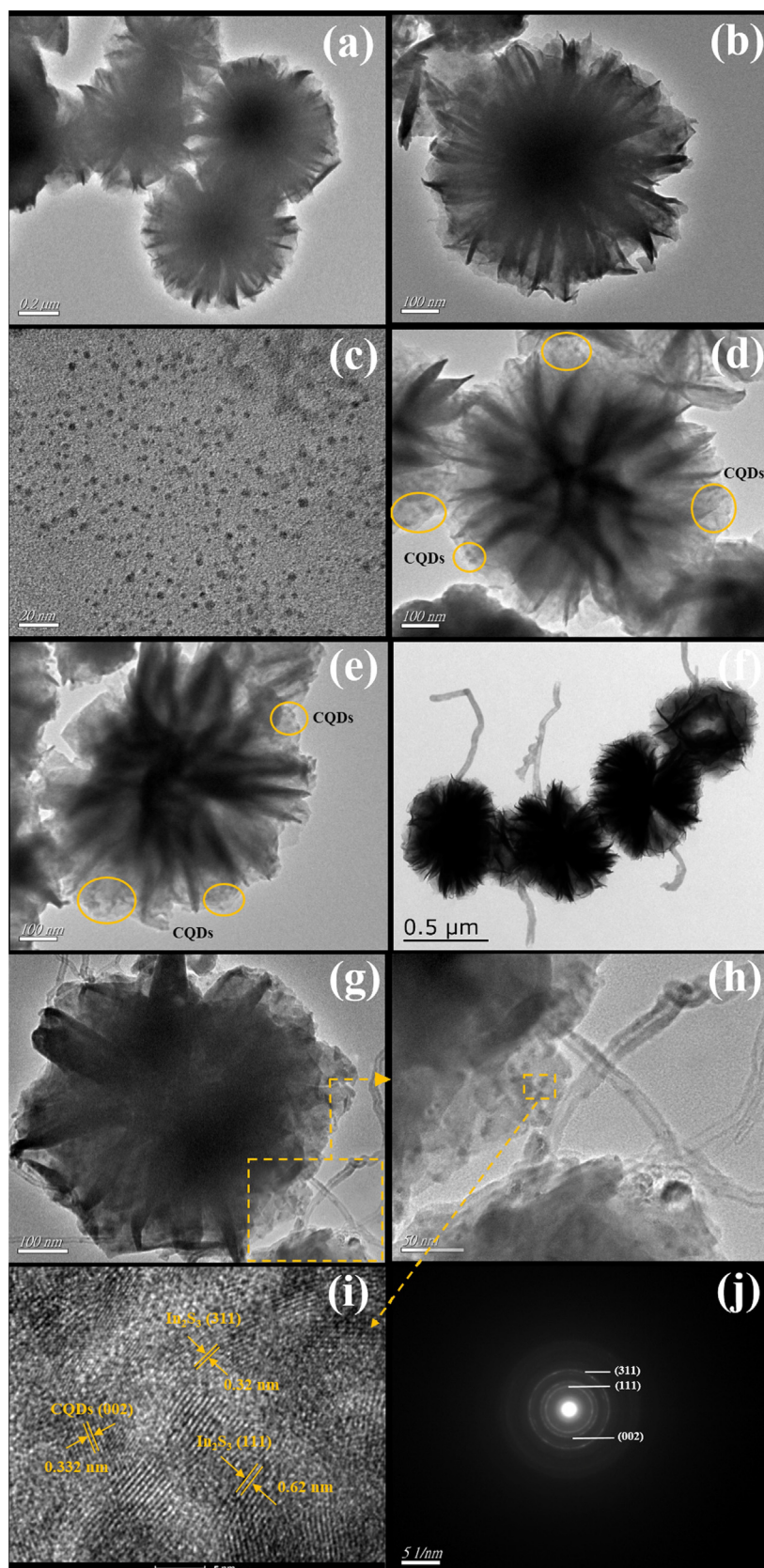
Fig. 3. TEM spectra of (a, b) bare β-In$_2$S$_3$, (c) CQDs, (d, e) In$_2$S$_3$/SWNTs, (f-h) CQDs@In$_2$S$_3$/SWNTs, (i) corresponding HR-TEM image of (h) marked in yellow and (j) SAED of CQDs@In$_2$S$_3$/SWNTs composites. (For interpretation of the references to colour in this figure legend, the reader is referred to the web version of this article.)
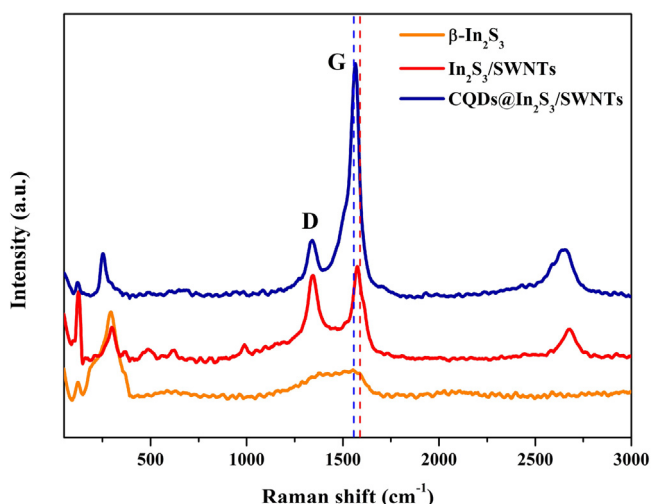
Fig. 4. Raman spectra of β-In_2S_3, In_2S_3/SWNTs and CQDs@In_2S_3/SWNTs.

In_2S_3 nanoflowers and SWNTs simultaneously which effectively connected the interfaces of each part and significantly increased the specific surface area, thus reveal the more obvious advantage of CQDs in CQDs@In_2S_3/SWNTs system. The formation of composite nanomaterials was further proved by HRTEM (Fig. 3i). Besides the lattice fringe spacings of 0.332 nm correspond to the (002) crystal plane of CQDs, two types of clear lattice fringes ca. 0.32 nm and ca. 0.62 nm, which correspond to (311) and (111) planes of the cubic β-In_2S_3 [21] of the XRD results(JCPDS 65-0459). The SAED pattern (Fig. 3j) also displayed three kinds of characteristic spots, further confirming the formation of CQDs@In_2S_3/SWNTs with layer-stacking heterostructures [37].

The EDS was carried out on a single nanoclusters in order to accurately investigate the nanoscale elemental composition as well as the spatial uniformity of the elemental distribution as shown in the inset of Fig. S1, which shows the CQDs@In_2S_3/SWNTs sample contain C, In and S element. The mass and atomic ratios of In, S and C element of as-obtained samples were given in Table S1. It further proves that the sample synthetized is CQDs@In_2S_3/SWNTs composite material. The Au peaks originated from the sputter coating to increase the conductivity for SEM measurements.

3.3. Raman spectroscopy

Raman spectroscopy was utilized to characterize the intrinsic structure of as-prepared products (Fig. 4). In_2S_3 has the orthorhombic structure composed of four molecules in a primitive unit cell and belongs to the space group Pmnn. According to the group theory, there should be 24 fundamental phonon modes [67]: $\Gamma = 4A_g$ $+2A_u + 4B_{1g} + 2B_{1u} + 2B_{2g} + 4B_{2u} + 2B_{3g} + 4B_{3u}$. Thus, there are 12 Raman active modes in In_2S_3 given by $4A_g + 4B_{1g} + 2B_{2g} + 2B_{3g}$. Here in, in the Raman spectra of β-In_2S_3, two strong peaks at 157 and 272 cm^{-1} assigned to the LO peaks, and other two weak peaks at 232 and 474 cm^{-1} can be attributed to LO phonon overtone peaks, respectively [68]. Common features were present in 1000–2000 cm^{-1} region, where the D-band peaking at 1350 cm^{-1} and the G-band peaking at 1590 cm^{-1} reflects the disorder or defects in the graphitized structure. The intensity ratios of the D- to G-bands (I_D/I_G) for In_2S_3/SWNTs and CQDs@In_2S_3/SWNTs were 0.98 and 0.23, respectively [22]. The existent intensity enhancement of G-band peak mainly resulted from surface oxidation and internal stretching vibration of Sp2 hybridization of Carbon atom, which caused by the introduction of CQDs. Furthermore, it can be observed from Fig. 4 that the G peak of CQDs@In_2S_3/SWNTs composites shifts in a low-wavelength direction from ca. 1590 cm^{-1} to

1587 cm^{-1}, which further proves the strong interaction between CQDs and In_2S_3 [33,43].

3.4. UV–vis diffuse reflectance spectra

The photocatalytic efficiency is highly related to light absorption properties which were carried out by UV–vis diffuse reflectance spectra (DRS) as shown in Fig. 5. The sample of pure In_2S_3 exhibits a wide range of light absorption with an absorption edge at about 610 nm in visible-light region, corresponding to the band gap (E_g) of about 2.0 eV (Fig. 5b) which calculated via the transformation according to the Kubelka-Munk of $(\alpha h\nu)^{1/2} = A (h\nu - E_g)$ [11] for direct transition semiconductor, where α represents the absorption coefficient, h is Planck's constant, ν is the light frequency, A is a constant and E_g is the band gap energy. The shape indicates that the absorption relevant to the band gap is related to the intrinsic transition of semiconductor and not to the transition from impurity levels [14]. It can be seen that addition of SWNTs and CQDs have remarkable influences on the optical property of visible light absorption for the series of as-prepared nanocomposites, which the absorption edge of CQDs@In_2S_3/SWNTs sample showed significant red-shifts from ~610 nm to ~790 nm and the absorption intensity in the range of 610–800 nm for In_2S_3/SWNTs and CQDs@In_2S_3/SWNTs nanocomposites is all enhanced compared with pure In_2S_3 nanoflowers. As calculated in Fig. 5b, the band gap of In_2S_3/SWNTs and CQDs@In_2S_3/SWNTs were narrowed to 1.87 and 1.75 eV (Table 1). Therefore, coupling In_2S_3 nanoflowers with SWNTs and CQDs have significantly extended the absorption range may attribute to the formation of more photogenerated electron-hole pairs [15,64], which lead to better photocatalytic efficiency under visible-light irradiation.

3.5. BET measurements

To further investigate the role of SWNTs and CQDs on enhancing the photocatalytic activity of CQDs@In_2S_3/SWNTs nanocomposite, the Brunauer-Emmett-Teller (BET) gas-sorption measurements were performed. N_2 adsorption-desorption isotherms and the corresponding Barrett-Joyner-Halenda (BJH) pore-size distribution of pure β-In_2S_3 prepared at 180 °C for 10 h, In_2S_3-10% SWNTs and In_2S_3-10% SWNTs–10 mL CQDs have been displayed in Fig. 6. According to the IUPAC classification [17,69], the samples exhibited a typical type IV isotherm with a typical H3 hysteresis loop in the relative pressure (p/p_0) range of 0.2–0.8 [70], suggesting the existence of mesopores. The relationship between morphology and specific surface areas are listed in Table 1. The specific BET surface area and total pore volume are 40.637 m^2 g^{-1} and 0.197 cm^3 g^{-1} for pure daisy-like β-In_2S_3, 78.354 m^2 g^{-1} and 0.266 cm^3 g^{-1} for In_2S_3- 10% SWNTs, and 82.276 m^2 g^{-1} and 0.285 cm^3 g^{-1} for In_2S_3- 10% SWNTs–10 mL CQDs. As is clearly seen that the introduction of SWNTs and CQDs increase the BET surface area and total pore volume of In_2S_3. All of the results indicate that the CQDs and SWNTs have well combined with In_2S_3 nanoflowers and the increased specific surface areas are advantageous for absorb more active species and reactants on their surface, which thus benefit the enhancement of photocatalytic performance.

3.6. Photoluminescence spectra and FL analysis

To determine more detailed information about the effect of CQDs and SWNTs addition in the as-obtain nanocomposite, the efficiency of charge migration and transfer can be reflected by the excitation-dependent PL behavior which is closely related to the optical properties of photocatalysts. As shown in Fig. 7a, it is easy to observe that the PL spectra for pure β-In_2S_3, In_2S_3/SWNTs and CQDs@In_2S_3/SWNTs composites are all showing a strong emission
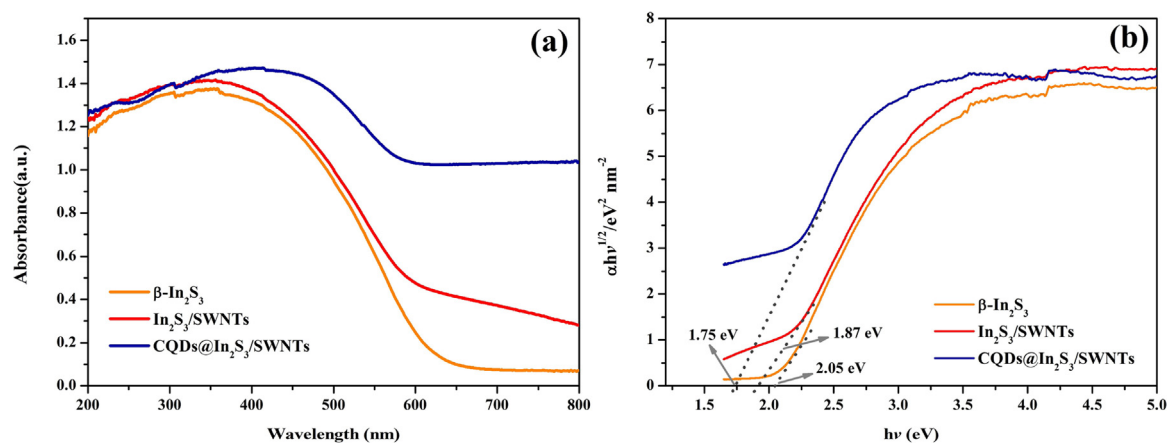
Fig. 5. (a) UV–vis diffuse reflectance spectra of β-In$_2$S$_3$, In$_2$S$_3$/SWNTs and CQDs@In$_2$S$_3$/SWNTs composite photocatalysts. (b) The corresponding plot of $(\alpha h\nu)^{1/2}$ vs. hν.

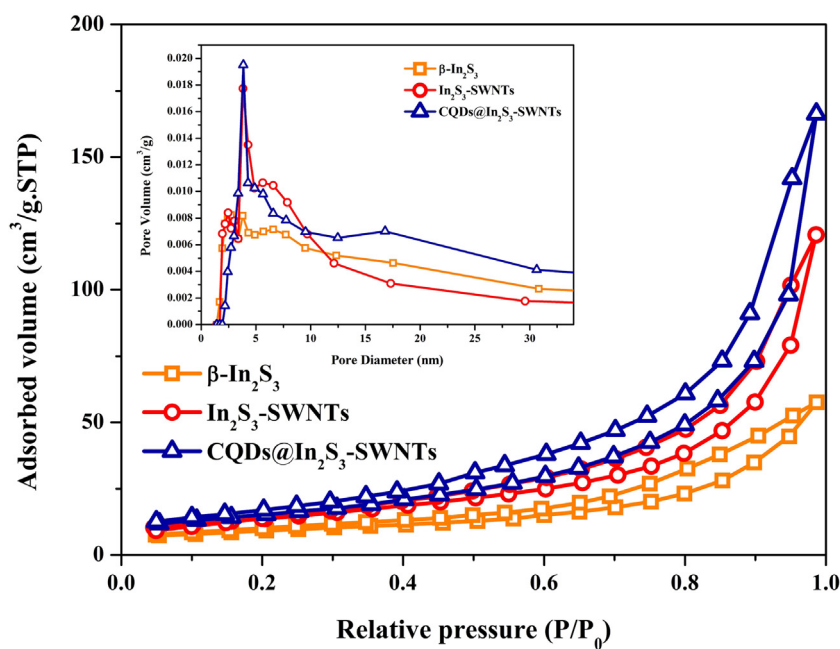**Fig. 6.** N$_2$ adsorption-desorption isotherm of β-In$_2$S$_3$, In$_2$S$_3$/SWNTs and CQDs@In$_2$S$_3$/SWNTs, inset is corresponding pore-size distribution curves.
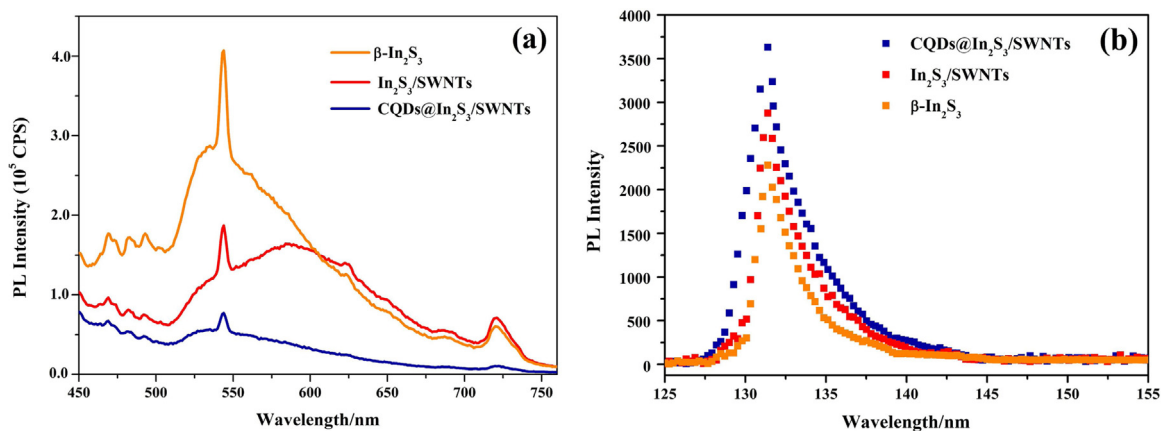
Fig. 7. Solid PL emission spectra (a) and FL emission decay (b) of β-In$_2$S$_3$, In$_2$S$_3$/SWNTs and CQDs@ In$_2$S$_3$/SWNTs, excited at 420 nm.
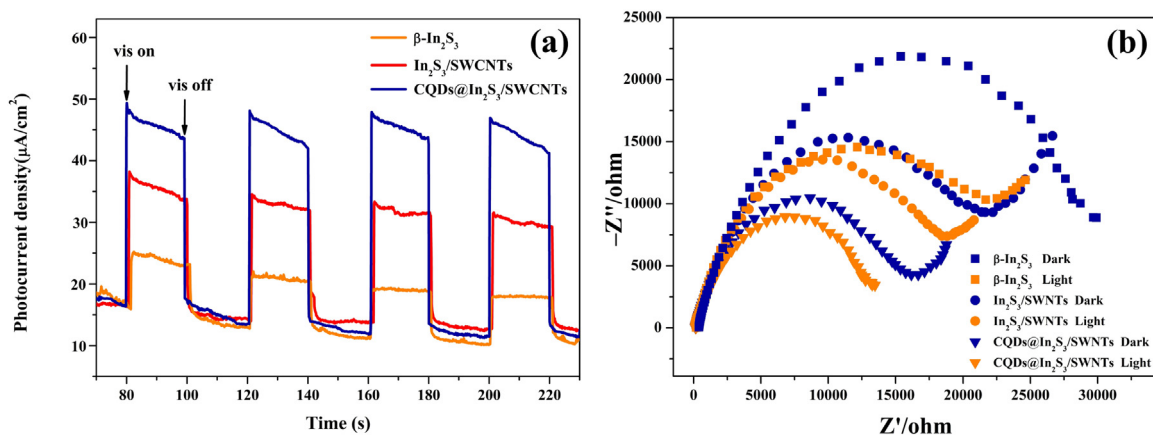
Fig. 8. (a) Transient photocurrent response of β-In_2S_3, In_2S_3/SWNTs and CQDs@In_2S_3/SWNTs nanocomposite under visible-light irradiation (Init E = 0.5 V, [Na_2SO_4] = 0.5 M). (b) EIS spectra of β-In_2S_3, In_2S_3/SWNTs and CQDs@In_2S_3/SWNTs in the light and dark (Init E = 0.5 V, [Na_2SO_4] = 0.5 M).

Table 2
Corresponding calculation results for radiative lifetime of the fitting decay curves.

	β-In_2S_3	In_2S_3/SWNTs	CQDs@In_2S_3/SWNTs
radiative lifetime	2.38 ns	2.21 ns	1.83 ns

peak under an excitation wavelength of 420 nm addition of CQDs will lead to PL quenching [17]. In particular, CQDs@In_2S_3/SWNTs composites exhibit significantly lower PL intensity as compared to the pure β-In_2S_3, In_2S_3/SWNTs nanomaterial, indicating that the recombination of the photogenerated electron-hole pairs is most efficiently inhibited greatly in the CQDs@In_2S_3/SWCNT composites, which attributed to the intimate interfacial contact of In_2S_3 with SWNTs and CQDs and the modification with CQDs and SWNTs can prolong electron-hole pair lifetime [71].

In order to investigate the further examination of charge carrier mobility, the transient fluorescence were introduced and analyzed. According to the calculation for the radiative lifetime of fitting decay curves (Table 2) [72], the results are 2.38, 2.21 and 1.83 ns for β-In_2S_3, In_2S_3/SWNTs and CQDs@In_2S_3/SWNTs, respectively. As is known, the relative shorter decay lifetime of the excitation states presented faster interfacial electron transfer occurring at the interfacial attachments of semiconductors and carbon materials which can cause the relative greater separation rate of photogenerated e^-/h^+ pairs [43]. What is more, the quenched photoluminescence and the reduced decay lifetime further illuminate the greater separation of photogenerated electrons and holes occurring at the interfaces of the compounds. In contrast, the relative faster charge recombination will induce a higher photoluminescence [31]. We can see from Fig. 7b that the CQDs@In_2S_3/SWNTs with the shortest decay time be provided with a best ability for separating photogenerated e^-/h^+ pairs and efficiently utilize the charge carriers as SWNTs and CQDs. Meanwhile, the highest efficient in charge transfer and separation occurring in the ternary heterostructure system which lead to the huge improvement of photocatalytic activity and inhibit the charge recombination [73]. The results indicate that the multicomponent heterostructures of CQDs@In_2S_3/SWNTs can effectively enhance the excitons separation at the interfaces and transfer of photoexcited electrons among In_2S_3, SWNTs and CQDs.

3.7. Electrochemical properties

To further identify the introduction of CQDs can favor the effective charge transfer in the as-obtained composite system and reduce the electrons and holes recombination rate thus improve

the photocatalytic activities [28], the photoelectrochemical experiments are always performed. As a powerful method to demonstrate the visible light response of as-prepared photocatalysts, the transient photocurrent responses of pure In_2S_3, In_2S_3/SWNTs and CQDs@In_2S_3/SWNTs composites are recorded for four on-off cycles under visible-light irradiation ($\lambda > 420$ nm) in a chopping mode and the photocurrent-time (*I-t*) curves are displayed in Fig. 8a. It can be observed from working electrodes that the photocurrent density is obviously enhanced whenever the visible-light irradiation is activated. As expected, the CQDs@In_2S_3/SWNTs composite photocatalyst shows the highest photocurrent intensity of the three samples, whereas In_2S_3/SWNTs and pure In_2S_3 possess the middle and lowest values, respectively. The photocurrent is formed mainly by diffusion of the photogenerated electrons to the back contact, while the photoinduced holes are taken up by the holes acceptor in the electrolyte. The enhanced photocurrent of as-prepared CQDs@In_2S_3/SWNTs indicates the more efficient separation and longer lifetime of charge carriers over it than that of In_2S_3/SWNTs and pure In_2S_3, which is consistent with the PL and DRS spectra. It could be attributed to the introduction of CQDs and SWNTs. In fact, although the classical quantum confinement found in semiconductor QDs is not applicable in carbon dots, as the emission colors in the latter are associated with different trapping sites and/or recombination paths of the electrons and holes, the small size for the core carbon nanoparticles like CQDs is required for an extremely large surface-to-volume ratio to ensure a large population of diverse surface defect sites [64]. Meanwhile, the CQDs is considered to be a good electron acceptor material owe to the conjugated π structure, and acted as the separation center of the phoroexcited charge carriers [25]. Furthermore, the photogenerated electrons are excited from the VB to the CB of In_2S_3 and then transfer to the SWNTs and CQDs, suggesting the life span of photogenerated charge carriers can be remarkably boosted by the strategy of increasing the interfacial contact among In_2S_3, SWNTs and CQDs.

In addition, the electrochemical impedance spectroscopy (EIS) Nyquist analysis has also been carried out to examine the influence of interfacial charge carrier dynamics after the CQDs and SWNTs were introduced in In_2S_3 based photocatalysts system without and with visible light irradiation. As shown in Fig. 8b, Nyquist plots of In_2S_3/SWNTs and CQDs@In_2S_3/SWNTs electrode materials cycled in 0.5 M Na_2SO_4 electrolyte solution and all show semicircles at high frequencies. It is known that the high-frequency in the EIS spectra are corresponds to the charge transfer limiting process which can be attributed to the charge transfer resistance at the contact interface between the electrode and the electrolyte solu-
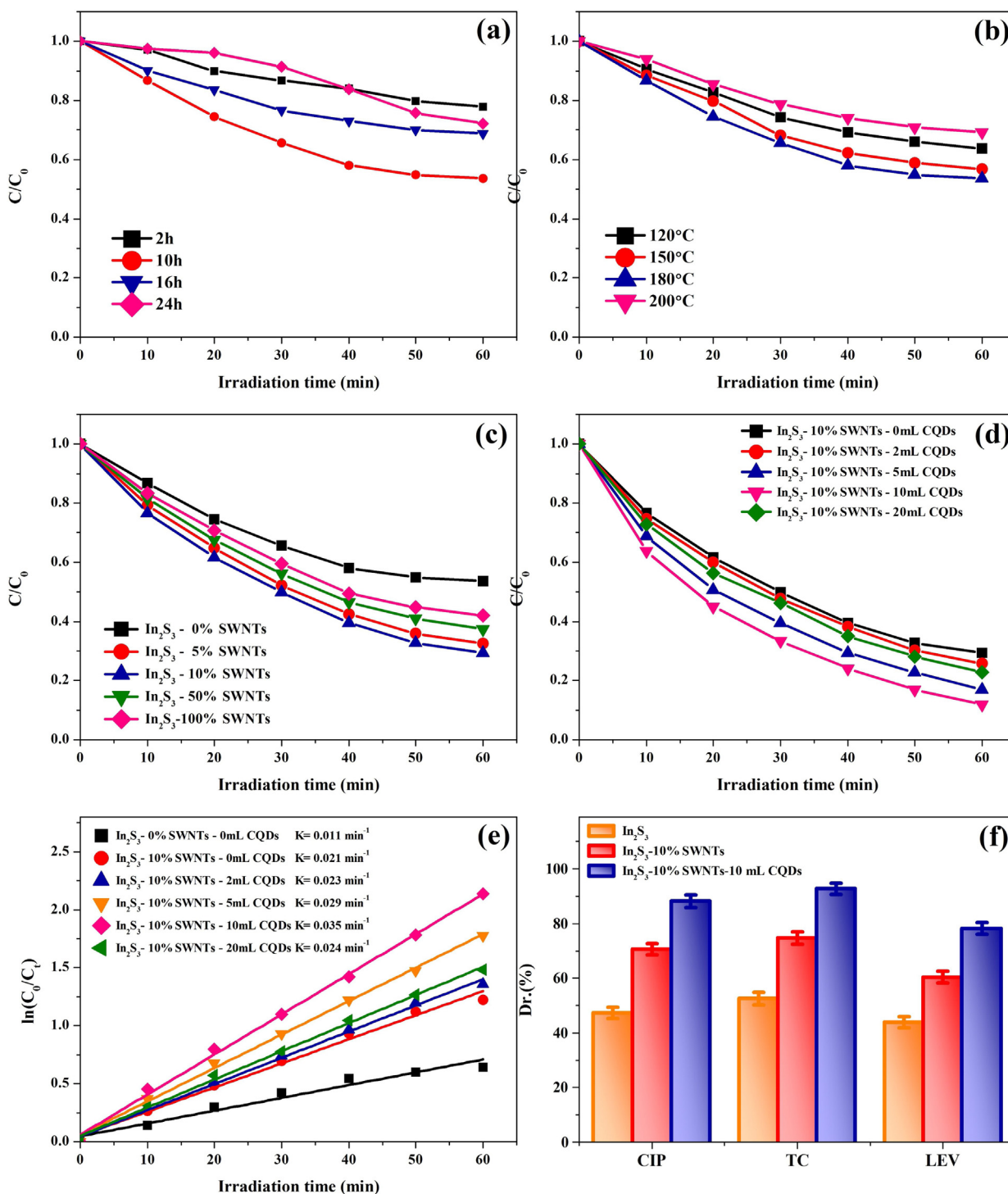
Fig. 9. (a – d): Photocatalytic degradation of CIP with different synthesis conditions and different mass ratio of SWNTs and CQDs under visible-light irradiation. (e) pseudo-first-order kinetic plots of $\ln(C_0/C_t)$ as a function of visible irradiation time for photocatalysis of CIP containing bare In_2S_3, In_2S_3/SWNTs and In_2S_3/SWNTs with different amounts of CQDs. (f) Contrastive photodegradation rates of CIP, TC and LEV over In_2S_3-10% SWNTs–10 mL CQDs for 60 min under visible light irradiation.

tion, and the charge transfer resistance can be directed analyzed by the semicircle radius [74]. The smaller arc radius of the EIS Nyquist plot represents the lower charge transfer resistance [75]. Consequently, the smaller arc of CQDs@In_2S_3/SWNTs as compared to that both of β-In_2S_3 and In_2S_3/SWNTs implies that the modification of CQDs and SWNTs have accelerated interfacial electron transfer and improved the charge separation efficiency at the electrode interface. After the visible light irradiation, the Nyquist plots of as-

obtained photocatalysts are smaller than that in the dark, indicating that the impedance have been weakened which due to the higher separation rate of photogenerated e^-/h^+ pairs and the faster charge migration velocity after the irradiation [76]. All of above results imply that the introduction of CQDs can obviously favor the separation and transfer of photogenerated carriers in CQDs@In_2S_3/SWNTs composites and then enhance the photocatalytic activity.
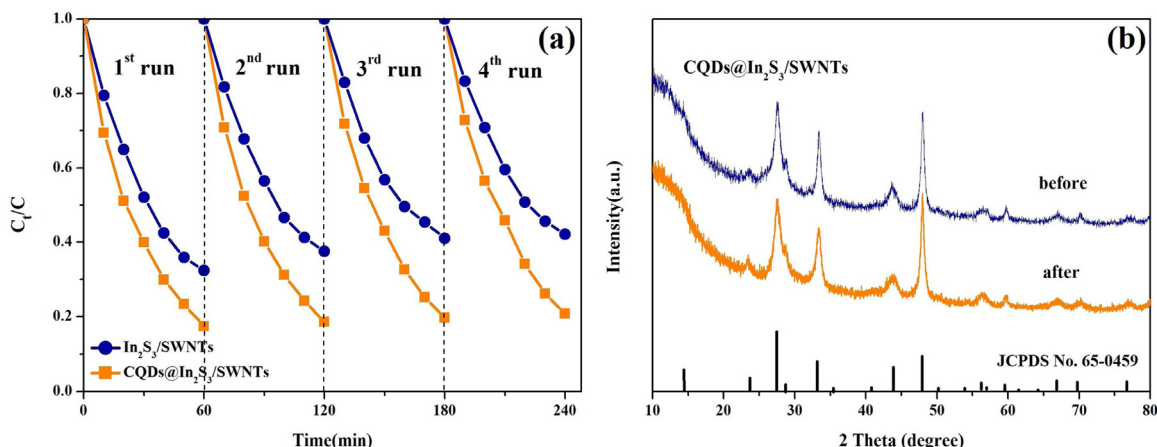
Fig. 10. (a) Cycling experiments for the photocatalytic degradation of ciprofloxacin by the prepared In_2S_3/SWNTs and 10 mL CQDs@In_2S_3-10% SWNTs composite under visible-light irradiation. (b) XRD patterns of CQDs@In_2S_3/SWNTs before and after photocatalytic degradation of ciprofloxacin for the fourth cycle.

3.8. Photocatalytic activity measurements

3.8.1. Photocatalytic activity study

The optimization of the amount and synthesis conditions of photocatalyst were investigated to improve the photocatalytic activity of as-prepared photocatalysts, which evaluated by photodegrading three different kinds of pollutants, namely, CIP ($10\,mg\,L^{-1}$), TC ($20\,mg\,L^{-1}$) and LEV ($15\,mg\,L^{-1}$) as model pollutants under visible light irradiation. The changes of CIP, TC and LEV concentration at different time intervals were investigated by measuring the absorption in UV–vis spectra at 276 nm, 357 nm and 287 nm, respectively. The adsorption-desorption balance was achieved between the photocatalysts and contaminants for 30 min absorption process in the dark before irradiating by visible light. The photocatalytic efficiency is defined as C_t/C_0, where C_0 corresponds to the initial concentration of the pollutants after dark adsorption and C_t is the rest of concentration after visible light irradiation for the certain period. As shown in Fig. 9a–d, it was found that the best photocatalytic performance of CQDs@In_2S_3/SWNTs was obtained with a certain content as In_2S_3-10% SWNTs–10 mL CQDs which fabricated at 180 °C for 10 h. We can see from Fig. 9c that 47% CIP can be removed by pure In_2S_3 materials in 60 min visible light irradiation. With the introduction of different amounts of shorted, functional SWNTs to the In_2S_3, the photocatalytic activity have improved and peaked at 10 wt% of SWNTs. When the CQDs was introduced to the as-obtained In_2S_3/SWNTs composite, a remarkable enhancement of 27% of photocatalytic activity has been exhibited compared with In_2S_3/SWNTs after 60 min irradiation. This indicated that the CQDs modification was an efficient way to improve the photocatalytic performance of In_2S_3/SWNTs. With an increase in the different amount of CQDs, the photodegradation of CQDs@In_2S_3/SWNTs material displayed an increasing trend and the 10 mL CQDs/In_2S_3/10 wt% SWNTs hybrid material exhibits the highest activity of CIP photodegradation which reached 89%. However, when the CQDs content was higher than 10 mL, the increase of CQDs content caused a decrease for the photocatalytic activity. The reason is that although the modification of CQDs to In_2S_3 and SWNTs was favorable for charge transfer from In_2S_3/SWNTs, too many CQDs cover on the surface of In_2S_3 would limit the light absorption of photocatalytic semiconductor and reduce the contact area between the pollutant and as-prepared photocatalysts. The similar results have been also proposed in relative literatures [45,61,77]. Fig. 9e shows a linear relationship between ln (C_0/C_t) and reaction time, indicating that the photodegradation of CIP follows first-order kinetics [78]. The pseudo-first-order rate constants (k) for different photocatalysts at room temperature are calculated

from the slope [71]. The apparent rate constants were determined as 0.011, 0.021 and 0.035 min^{-1} for β-In_2S_3, In_2S_3–10 wt% SWNTs and In_2S_3–10 wt% SWNTs–10 mL CQDs, respectively. In either case, the arrival times of the electrons and holes at the surface of compounds are separated, thereby suppressing the recombination of photogenerated charges. Moreover, the bright surface defect-derived fluorescence of CQDs is due to the recombination of electron-hole pairs in the strongly localised π and π* electronic levels of the sp^2 sites [42,64], these sites leading to strong visible emissions and serve as a recombination site for the photogenerated electron and holes [35]. The accordant conclusion could also be observed in PL analysis (Fig. 7). Therefore, the photocatalytic activity of CQDs@In_2S_3/SWNTs could be enhanced attribute to the presence of CQDs as more charge carriers and excitors are available. Based on Fig. 9f and above discussion, it can be accepted that the 10 mL CQDs@In_2S_3/10% SWNTs sample achieves the highest activity for the photodegradation of CIP, TC and LEV.

3.8.2. Stability

It is known that stability and reusability are very important evidence to judge the quality of photocatalyst and for the further environmental application. The CQDs@In_2S_3/SWNTs composites also have a favorable cycle performance, which has been demonstrated by four successive recycling experiments for photocatalytic degradation of CIP over the samples of In_2S_3/SWNTs and CQDs@In_2S_3/SWNTs. The test results were shown in Fig. 10. We can see clearly that during four recycles of photoactivity test for degradation of CIP under visible light irradiation, the photocatalytic efficiency of CQDs@In_2S_3/SWNTs displays a slight decrease and shows almost no deactivation. It is noteworthy that there is a remarkable enhancement of photoactivity of CQDs@In_2S_3/SWNTs composite material compared with the In_2S_3/SWNTs, indicating that the introduction of CQDs can efficiently inhibit the photocorrosion and deactivation of the In_2S_3 nanoflowers. For the further investigation of stability of as-prepared photocatalysts, the XRD analysis of 10 mL CQDs@In_2S_3/10% SWNTs before and after four consecutive experiments for degradation of CIP solution are displayed in Fig. 10(b). The main characteristic diffraction peaks of CQDs@In_2S_3/SWNTs are in almost the same positon from the pattern, which present the crystal structure is unchanged after cycling tests. And the intensity of photocatalysts with a slight decrease as compared with the sample before repeated photodegradation. Therefore, the as-prepared CQDs@In_2S_3/SWNTs can be identified as a stable VLD photocatalysts with the addition of CQDs as the charge carrier and photoactive protective layer on the surface of photocatalysts.
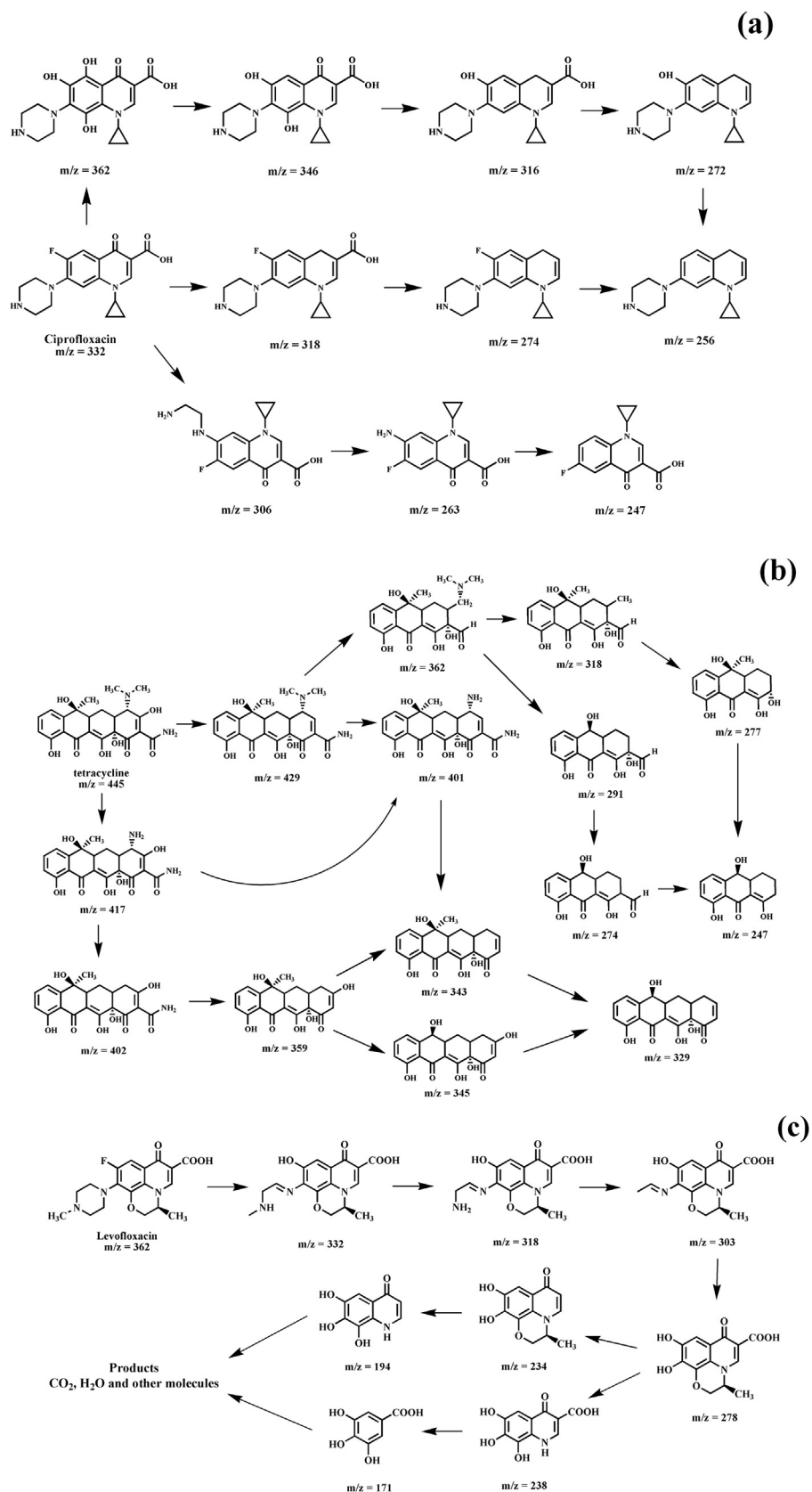
Fig. 11. The proposed intermediate products of photodegradation of (a) ciprofloxacin, (b) tetracycline and (c) levofloxacin irradiated by visible light.
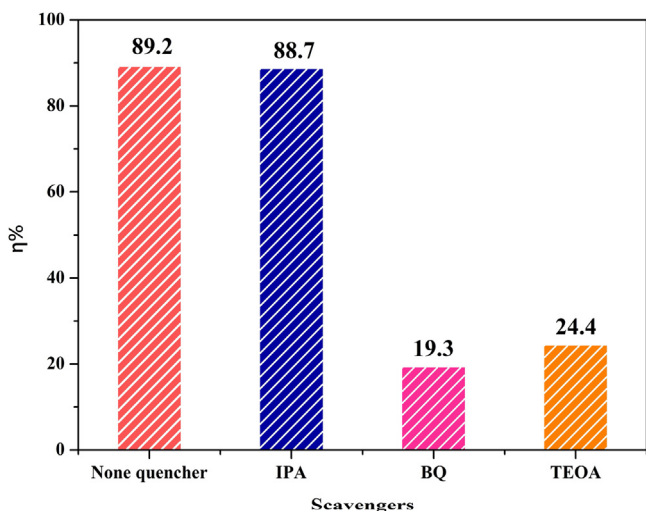
Fig. 12. Trapping experiment of active species during the photocatalytic degradation of CIP over CQDs@In$_2$S$_3$/SWNTs photocatalyst under visible light irradiation.

3.9. Mass spectral analysis

In order to investigate the further identification of the ciprofloxacin, tetracycline and levofloxacin intermediates during the photodegradation process, the Mass spectrometry (MS) is examined and the corresponding analysis of the adsorption in the dark for 0.5 h, photodegradation for 0.4 h and 1 h of CIP, TC and LEV are shown in Fig. S2. The protonated CIP, TC and LEV molecular ions were detected by the major reactive oxidated species with m/z 445.33, m/z 332.32 and m/z 362.34, respectively. The relative sequence of successive ions fragmentations during collision-induced dissociation were analyzed. The proposed degradation products and reaction pathways of CIP, TC and LEV were displayed in Fig. 11–c. All above analyses demonstrated that the initial antibiotic molecules and intermediate products may be degraded to CO_2, H_2O and other molecules.

3.10. Mechanism of pollutant photodegradation

3.10.1. Active species trapping and quantification experiments

To determine the roles of the active species during the photocatalysis process over CQDs@In$_2$S$_3$/SWNTs materials, a series of active species trapping and quantification experiments were then investigated by adding different trapping scavengers. Isopropyl alcohol (IPA) for •OH, p-benzoquinone (BQ) for O_2•$^-$ and triethanolamine (TEOA) for holes [5]. As shown in Fig. 12, the photodegradation of CIP was not affected when the IPA was added, which indicated that the •OH was not the main active species. On the contrary, the photocatalytic activity was greatly inhibited when

the BQ and TEOA were added. These indicated that the O_2•$^-$ and h$^+$ played the principal roles during the photodegradation process.

3.10.2. ESR behavior analysis

To further reveal the main active species during the photocatalysis process, the electron spin resonance (ESR) spin-trap technique with 5,5-diamethyl-1-pyrroline N-oxide (DMPO) and 4-oxo-2,2,6,6-tetramethyl (4-oxo-TEMP) was introduced to further verify the presence of •OH, O_2•$^-$ and 1O_2 radicals of CQDs@In$_2$S$_3$/SWNTs photocatalysts under visible light irradiation [59]. As shown in Fig. 13, there are no obvious DMPO-•OH signal appeared, indicating that the •OH cannot be generated in both In$_2$S$_3$/SWNTs and CQDs@In$_2$S$_3$/SWNTs systems (Fig. 13a). In Fig. 13b, six characteristic peaks of DMPO—O_2•$^-$ appear in the spectra after visible light irradiation, revealing that the photogenerated electrons in the conduction band of semiconductors can be transformed into O_2•$^-$ radicals during the photodegradation system [79]. From the peak of In$_2$S$_3$/SWNTs without CQDs with the weaker intensity it can be concluded that after the introduction of CQDs, the increasing charge separation have promoted CQDs@In$_2$S$_3$/SWNTs to effective utilization of electrons to produce more O_2•$^-$. Meanwhile, the singlet oxygen (1O_2), which generated from the reaction between electrons and holes plays an important role in aerobic degradation [80]. The 1O_2 radicals of CQDs@In$_2$S$_3$/SWNTs photocatalyst systems were detected by adding 10 mM 4-oxo-TEMP in aqueous solution under visible light irradiation. The TEMPONE• signals were produced and the distinctive trident ESR response can be observed from Fig. 13c. Comparing with the ESR signal in dark, a typical line spectrum with a strong intensity for TEMPONE• was detected when the visible light added into the irradiated-catalysts system. What is more, abundant O_2•$^-$ which generating under light irradiation can also react h$^+$ to produce 1O_2[43,59]. The result of the ESR analysis was consistent with active species trapping experiments. Therefore, according to the above analysis, we can conclude that the O_2•$^-$, h$^+$ and 1O_2 are the active species of photocatalysts in the photocatalytic degradation reaction.

3.10.3. Proposed mechanism in the photodegradation system

On the basis of the above analysis, a proposed mechanism for the efficient visible light degradation of contaminants observed here is discussed to explain the enhancement of the photocatalytic activity of CQDs@In$_2$S$_3$/SWNTs composites. As shown in Fig. 14, the In$_2$S$_3$ with narrow band gap energy can be easily excited by visible light and produces electron-hole pairs [81]. A large number of free generated electrons in the conduction band (CB) and holes in the valence band (VB). The band edges of the In$_2$S$_3$ semiconductor were theoretically calculated by the empirical formulas $E_{VB} = X - E_e + 0.5E_g 0.5E_g$ and $E_{CB} = E_{VB} - E_g$ [3]. According to the band gap of In$_2$S$_3$ acquired from the DRS analysis (Fig. 5b) was 2.05 eV. As the X which represents the Mulliken electronegativity of the component atoms in In$_2$S$_3$ semiconductor is approximately 4.71 eV, the CB and VB energy of as-obtained In$_2$S$_3$ material were calculated
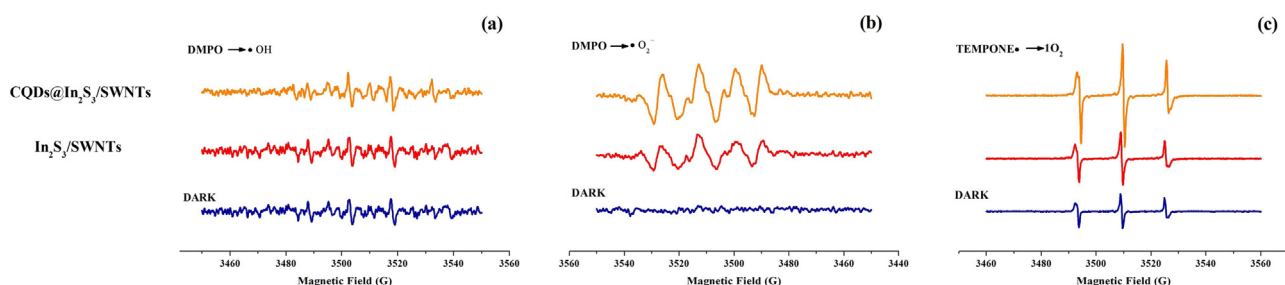

Fig. 13. DMPO and TEMP spin-trapping ESR spectra with 0.1 mg/mL In$_2$S$_3$/SWNTs and CQDs@In$_2$S$_3$/SWNTs samples in the dark and under visible light irradiation for 70 s at ambient temperature. For DMPO-•OH in aqueous dispersion (a), DMPO-O_2•$^-$ in methanol dispersion (b), and TEMPONE-•1O_2 in aqueous dispersion (c).
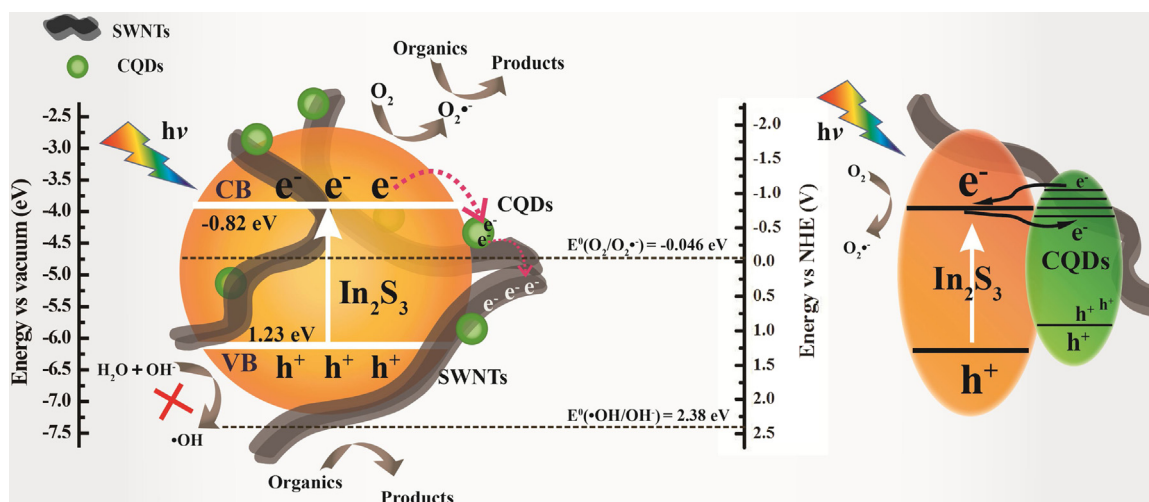
Fig. 14. A schematic of the proposed photocatalytic mechanism of organic contaminant degradated by CQDs@In$_2$S$_3$/SWNTs composites under visible light irradiation.

to be −0.82 eV and 1.23 eV (vs normal hydrogen electrode (NHE)). Since the CB value of In$_2$S$_3$ was more negative than E^0 (O$_2$/O$_2$•$^−$) (−0.046 eV vs NHE) and the VB value of In$_2$S$_3$ was more positive than E^0 (•OH/OH$^−$) (2.38 eV vs NHE)[66], indicated that the O$_2$ can be reduced by photogenerated electrons but the photogenerated holes of In$_2$S$_3$ cannot oxidize OH$^−$ to yield •OH.

The band gap of CQDs@In$_2$S$_3$/SWNTs composites was determined to be ca. 1.75 eV from DRS analysis in Fig. 5, which is slightly narrower than In$_2$S$_3$/SWNTs (1.87 eV). Based on the DRS absorption spectra, there is a possibility of additional photoexcitation in the CQDs contributing to this process.There's no denying that the crucial role of the introduced CQDs for the enhancement of photocatalytic activity. The holes transfer to the surface of the CQDs, where they can also join in the oxidation reaction of H$_2$O to O$_2$[34], which the CQDs acting in this way as a photogenerated hole-acceptor has been observed previously in other CQD-based composite materials [36,64]. In the other hand, the introduction of CQDs could efficiently increase specific surface area of composites materials and strengthen the interface contact of In$_2$S$_3$-CQDs and In$_2$S$_3$-CNTs S-C heterostructures which accelerating the interfacial charge transfer in the CQDs@In$_2$S$_3$/SWNTs system [82]. Additionally, CQDs also increase the light absorbance and the wavelength dependent quantum efficiency is consistent with the absorbance spectrum [33], which was favor for producing more electron-hole pairs. Finally, the introduction of CQDs can effectively protect the present photocatalysts from suffering low efficiency and poor stability [61].

4. Conclusions

In summary, we have shown that the daisy-like In$_2$S$_3$ nanoflowers decorated with CQDs and SWNTs. The hierarchical, multi-dimensional CQDs@In$_2$S$_3$/SWNTs composites with S-C heterostructure were synthesized using a series of simple facile physical and chemical process. We demonstrate that the CQDs@In$_2$S$_3$/SWNTs composites are effective visible-light-driven photocatalysts for degradation of CIP, TC and LEV with high photocatalytic activities. Such capabilities of CQD@In$_2$S$_3$/SWNTs are attributable to the excellent light restriction properties of the multi-dimensional protruding structure, and superior charge transfer and separation capabilities of the CQDs. The use of these multi-dimensional heterostructure components of CQD@In$_2$S$_3$/SWNTs as a visible-responsive photocatalyst for antibiotics degradation is a novel application of carbon-based

nanomaterials, which also provide new configurations for designing high-performance photocatalysts.

Appendix A. Supplementary data

Supplementary data associated with this article can be found, in the online version, at http://dx.doi.org/10.1016/j.apcatb.2016.11.021.

References

[1] G.D. Wright, ACS Infect. Dis. 1 (2015) 80–84.
[2] P.J. Frappaolo, ACS Symp. Ser. 320 (1986) 100–111.
[3] M. Zhou, D. Han, X. Liu, C. Ma, H. Wang, Y. Tang, P. Huo, W. Shi, Y. Yan, J. Yang, Appl. Catal. B 172–173 (2015) 174–184.
[4] R. Wang, G. Jiang, Y. Ding, Y. Wang, X. Sun, X. Wang, W. Chen, ACS Appl. Mater. Interfaces 3 (2011) 4154–4158.
[5] J. Li, M. Zhou, Z. Ye, H. Wang, C. Ma, P. Huo, Y. Yan, RSC Adv. 5 (2015) 91177–91189.
[6] X. Guo, H. Zhu, Q. Li, Appl. Catal. B 160–161 (2014) 408–414.
[7] M. Zhou, J. Li, Z. Ye, C. Ma, H. Wang, P. Huo, W. Shi, Y. Yan, ACS Appl. Mater. Interfaces 7 (2015) 28231–28243.
[8] Y. Gong, P. Zhang, X. Xu, Y. Li, H. Li, Y. Wang, J. Catal. 297 (2013) 272–280.
[9] J. Xue, S. Ma, Y. Zhou, Z. Zhang, M. He, ACS Appl. Mater. Interfaces 7 (2015) 9630–9637.
[10] S. Cao, J. Low, J. Yu, M. Jaroniec, Adv. Mater. 27 (2015) 2150–2176.
[11] Y. Li, G. Chen, Q. Wang, X. Wang, A. Zhou, Z. Shen, Adv. Funct. Mater. 20 (2010) 3390–3398.
[12] Z.L. Wu, C.H. Wang, B. Zhao, J. Dong, F. Lu, W.H. Wang, W.C. Wang, G.J. Wu, J.Z. Cui, P. Cheng, Angew. Chem. Int. Ed. 55 (2016) 4938–4942.
[13] O. Martin, A.J. Martin, C. Mondelli, S. Mitchell, T.F. Segawa, R. Hauert, C. Drouilly, D. Curulla-Ferre, J. Perez-Ramirez, Angew. Chem. Int. Ed. 55 (2016) 6261–6265.
[14] W. Yang, L. Zhang, J. Xie, X. Zhang, Q. Liu, Tao Yao, S. Wei, Q. Zhang, Y. Xie, Angew. Chem. Int. Ed. 55 (2016) 6716–6720.
[15] K. Maeda, K. Ishimaki, Y. Tokunaga, D. Lu, M. Eguchi, Angew. Chem. Int. Ed. 55 (2016) 8309–8313.
[16] N. Chaudhari, L. Mandal, O. Game, S. Warule, D. Phase, S. Jadkar, S. Ogale, ACS Appl. Mater. Interfaces 7 (2015) 17671–17681.
[17] M.Q. Yang, B. Weng, Y.J. Xu, Langmuir 29 (2013) 10549–10558.
[18] X. Fu, X. Wang, Z. Chen, Z. Zhang, Z. Li, D.Y.C. Leung, L. Wu, X. Fu, Appl. Catal. B 95 (2010) 393–399.

[19] E. Dalas, S. Sakkopoulos, E. Vitoratos, G. Maroulis, L. Kobotiatis, J. Mater. Sci. 28 (1993) 5456–5460.
[20] W. Gao, W. Liu, Y. Leng, X. Wang, X. Wang, B. Hu, D. Yu, Y. Sang, H. Liu, Appl. Catal. B 176–177 (2015) 83–90.
[21] X. Zhang, C. Shao, X. Li, N. Lu, K. Wang, F. Miao, Y. Liu, J. Hazard. Mater. 283 (2015) 599–607.
[22] X. An, J.C. Yu, F. Wang, C. Li, Y. Li, Appl. Catal. B 129 (2013) 80–88.
[23] H. Wang, L. Zhang, Z. Chen, J. Hu, S. Li, Z. Wang, J. Liu, X. Wang, Chem. Soc. Rev. 43 (2014) 5234–5244.
[24] Y. Fan, W. Ma, D. Han, S. Gan, X. Dong, L. Niu, Adv. Mater. 27 (2015) 3767–3773.
[25] Z. Zhang, Y. Huang, K. Liu, L. Guo, Q. Yuan, B. Dong, Adv. Mater. 27 (2015) 5906–5914.
[26] L. Liao, H. Peng, Z. Liu, J. Am. Chem. Soc. 136 (2014) 12194–12200.
[27] J. Mu, C. Shao, Z. Guo, Z. Zhang, M. Zhang, P. Zhang, B. Chen, Y. Liu, ACS Appl. Mater. Interfaces 3 (2011) 590–596.
[28] T.T. Duong, Q.D. Nguyen, S.K. Hong, D. Kim, S.G. Yoon, T.H. Pham, Adv. Mater. 23 (2011) 5557–5562.
[29] S. Kaur, V. Bhalla, M. Kumar, ACS Appl. Mater. Interfaces 7 (2015) 16617–16624.
[30] W.J. Liu, H. Jiang, H.Q. Yu, Chem. Rev. 115 (2015) 12251–12285.
[31] X. Xu, Z. Bao, G. Zhou, H. Zeng, J. Hu, ACS Appl. Mater. Interfaces 8 (2016) 14118–14124.
[32] H. Zhang, L. Zhao, F. Geng, L.-H. Guo, B. Wan, Y. Yang, Appl. Catal. B 180 (2016) 656–662.
[33] L. Bao, C. Liu, Z.L. Zhang, D.W. Pang, Adv. Mater. 27 (2015) 1663–1667.
[34] H. Li, X. Zhang, D.R. MacFarlane, Adv. Energy Mater. 5 (2015) 1401077.
[35] S. Zhu, Q. Meng, L. Wang, J. Zhang, Y. Song, H. Jin, K. Zhang, H. Sun, H. Wang, B. Yang, Angew. Chem. Int. Ed. 52 (2013) 3953–3957.
[36] S.Y. Lim, W. Shen, Z. Gao, Chem. Soc. Rev. 44 (2015) 362–381.
[37] S. Zhuo, M. Shao, S.-T. Lee, ACS Nano 6 (2012) 1059–1064.
[38] K.A. Fernando, S. Sahu, Y. Liu, W.K. Lewis, E.A. Guliants, A. Jafariyan, P. Wang, C.E. Bunker, Y.P. Sun, ACS Appl. Mater. Interfaces 7 (2015) 8363–8376.
[39] B.C. Martindale, G.A. Hutton, C.A. Caputo, E. Reisner, J. Am. Chem. Soc. 137 (2015) 6018–6025.
[40] D. Mazzier, M. Favaro, S. Agnoli, S. Silvestrini, G. Granozzi, M. Maggini, A. Moretto, Chem. Commun. 50 (2014) 6592–6595.
[41] D. Mosconi, D. Mazzier, S. Silvestrini, A. Privitera, C. Marega, L. Franco, A. Moretto, ACS Nano 9 (2015) 4156–4164.
[42] L. Bao, Z.L. Zhang, Z.Q. Tian, L. Zhang, C. Liu, Y. Lin, B. Qi, D.W. Pang, Adv. Mater. 23 (2011) 5801–5806.
[43] R. Liu, H. Huang, H. Li, Y. Liu, J. Zhong, Y. Li, S. Zhang, Z. Kang, ACS Catal. 4 (2014) 328–336.
[44] H. Kang, Z. Zhou, M.L. Clarke, J.R. Simpson, J. Tang, A.R.H. Walker, J.T. Woodward, T. Nguyen, S.G. Chou, a.J. Hwang, ACS Nano 3 (2009) 3769–3775.
[45] N.C.T. Martins, J. Ângelo, A.V. Girão, T. Trindade, L. Andrade, A. Mendes, Appl. Catal. B 193 (2016) 67–74.
[46] T.C. Araújo, H.d.S. Oliveira, J.J.S. Teles, J.D. Fabris, L.C.A. Oliveira, J.P. de Mesquita, Appl. Catal. B 182 (2016) 204–212.
[47] J. Xia, J. Di, H. Li, H. Xu, H. Li, S. Guo, Appl. Catal. B 181 (2016) 260–269.
[48] M.S. Arnold, A.A. Green, J.F. Hulvat, S.I. Stupp, M.C. Hersam, Nat. Nanotechnol. 1 (2006) 60–65.
[49] Z.R. Hesabi, N.K. Allam, K. Dahmen, H. Garmestani, A.E.-S.M, ACS Appl. Mater. Interfaces 3 (2011) 952–955.
[50] M. Alsawat, T. Altalhi, K. Gulati, A. Santos, D. Losic, ACS Appl. Mater. Interfaces 7 (2015) 28361–28368.
[51] B. Czech, W. Buda, S. Pasieczna-Patkowska, P. Oleszczuk, Appl. Catal. B 162 (2015) 564–572.
[52] H. Shi, G. Li, H. Sun, T. An, H. Zhao, P.-K. Wong, Appl. Catal. B 158–159 (2014) 301–307.
[53] H. Wang, J. Li, M. Zhou, Q. Guan, Z. Lu, P. Huo, Y. Yan, J. Ind. Eng. Chem. 30 (2015) 64–70.
[54] C.Y. Chen, R.G. Zepp, Environ. Sci. Technol. 49 (2015) 13835–13843.
[55] J. Liu, A.G. Rinzler, H. Dai, J.H. Hafner, R.K. Bradley, P.J. Boul, A. Lu, T. Iverson, K. Shelimov, C.B. Huffman, F. Rodriguez-Macias, Y.-S. Shon, T.R. Lee, D.T. Colbert, R.E. Smalley, Science 280 (1998) 1253–1256.
[56] J. Zhang, H. Zou, Quan Qing, Y. Yang, Q. Li, Z. Liu, X. Guo, Z. Du, J. Phys. Chem. B 107 (2003) 3712–3718.
[57] K.J. Ziegler, Z. Gu, H. Peng, E.L. Flor, R.H. Hauge, R.E. Smalley, J. Am. Chem. Soc. 127 (2005) 1541–1547.
[58] J. Tian, P. Hao, N. Wei, H. Cui, H. Liu, ACS Catal. 5 (2015) 4530–4536.
[59] W. He, H. Jia, D. Yang, P. Xiao, X. Fan, Z. Zheng, H.K. Kim, W.G. Wamer, J.J. Yin, ACS Appl. Mater. Interfaces 7 (2015) 16440–16449.
[60] W. Wang, T.W. Ng, W.K. Ho, J. Huang, S. Liang, T. An, G. Li, J.C. Yu, P.K. Wong, Appl. Catal. B 129 (2013) 482–490.
[61] J. Di, J. Xia, M. Ji, B. Wang, X. Li, Q. Zhang, Z. Chen, H. Li, ACS Sustain. Chem. Eng. 4 (2016) 136–146.
[62] K.L. Chung, Y.H. Tsai, Comput. Math. Appl. 29 (1995) 109–113.
[63] X. Zhang, X. Li, C. Shao, J. Li, M. Zhang, P. Zhang, K. Wang, N. Lu, Y. Liu, J. Hazard. Mater. 260 (2013) 892–900.
[64] X. Li, M. Rui, J. Song, Z. Shen, H. Zeng, Adv. Funct. Mater. 25 (2015) 4929–4947.
[65] J. Kim, H. Hiroi, T.K. Todorov, O. Gunawan, M. Kuwahara, T. Gokmen, D. Nair, M. Hopstaken, B. Shin, Y.S. Lee, W. Wang, H. Sugimoto, D.B. Mitzi, Adv. Mater. 26 (2014) 7427–7431.
[66] J. Di, J. Xia, M. Ji, B. Wang, S. Yin, H. Xu, Z. Chen, H. Li, Langmuir 32 (2016) 2075–2084.
[67] K. KAMBA, J. SPYRIDELIS, M. BALKANSKI, Phys. Status Solidi B 105 (1981) 291.
[68] N.M. Gasanly, H. özkan, A. Aydinli, Ï Yilmaza, Solid State Commun. 110 (1999) 231–236.
[69] Y. Zhang, Z.-R. Tang, X. Fu, Y.-J. Xu, ACS Nano 5 (2011) 7426–7435.
[70] L.Y. Chen, Z.D. Zhang, W.Z. Wang, J. Phys. Chem. C 112 (2008) 4117–4123.
[71] S. Khanchandani, S. Kundu, A. Patra, A.K. Ganguli, J. Phys. Chem. C 117 (2013) 5558–5567.
[72] Y. Han, H. Huang, H. Zhang, Y. Liu, X. Han, R. Liu, H. Li, Z. Kang, ACS Catal. 4 (2014) 781–787.
[73] Z. Li, H. Yu, T. Bian, Y. Zhao, C. Zhou, L. Shang, Y. Liu, L.-Z. Wu, C.-H. Tung, T. Zhang, J. Mater. Chem. C 3 (2015) 1922–1928.
[74] L. Wu, J. Li, S. Zhang, L. Long, X. Li, C. Cen, J. Phys. Chem. C 117 (2013) 22591–22597.
[75] W. Zhou, W. Li, J.-Q. Wang, Y. Qu, Y. Yang, Y. Xie, K. Zhang, L. Wang, H. Fu, D. Zhao, J. Am. Chem. Soc. 136 (2014) 9280–9283.
[76] J. Di, J. Xia, Y. Ge, H. Li, H. Ji, H. Xu, Q. Zhang, H. Li, M. Li, Appl. Catal. B 168–169 (2015) 51–61.
[77] B. Long, Y. Huang, H. Li, F. Zhao, Z. Rui, Z. Liu, Y. Tong, H. Ji, Ind. Eng. Chem. Res. 54 (2015) 12788–12794.
[78] M. Zhou, X. Gao, Y. Hu, J. Chen, X. Hu, Appl. Catal. B 138–139 (2013) 1–8.
[79] W. He, H. Wu, W.G. Wamer, H.K. Kim, J. Zheng, H. Jia, Z. Zheng, J.J. Yin, ACS Appl. Mater. Interfaces 6 (2014) 15527–15535.
[80] Y. Liu, H. Wu, M. Li, J.J. Yin, Z. Nie, Nanoscale 6 (2014) 11904–11910.
[81] H. Wang, X. Yuan, Y. Wu, G. Zeng, H. Dong, X. Chen, L. Leng, Z. Wu, L. Peng, Appl. Catal. B 186 (2016) 19–29.
[82] X. Yu, J. Liu, Y. Yu, S. Zuo, B. Li, Carbon 68 (2014) 718–724.